Materials & Design 256 (2025) 114272

Contents lists available at ScienceDirect

Materials & Design

journal homepage: www.elsevier.com/locate/matdes

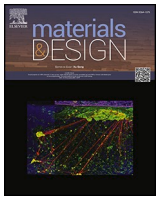

# Architecture-driven deformation and fracture behavior of nanolamellar TiN/Nb coatings

S. Kagerer [a], N. Koutná [a], L. Zauner [a], T. Wojcik [a], G. Habler [b], H. Riedl [a], P.H. Mayrhofer [a,*], R. Hahn [a]

[a] Institute of Materials Science and Technology, TU Wien, A-1060 Vienna, Austria
[b] Department of Lithospheric Research, University of Vienna, A-1090 Vienna, Austria

ARTICLE INFO

*Keywords:*
DFT
PVD
TiN/Nb multilayers
Hard coatings
Micromechanical compression tests
Confined layer slip model

ABSTRACT

Despite extensive studies on ceramic multilayers, combinations of nitrides with metals remain underexplored, particularly in the context of enhancing fracture resistance through interface design. In this study, we explore the mechanical and thermodynamic properties of 30 multilayered systems combining nitrides (XN) and carbides (XC) of group IV transition metals, X = {Ti, Zr, Hf}, with group V–VI high-temperature metals, M = {V, Nb, Ta, Mo, W}, using Density Functional Theory. Among them, TiN/Nb and TiN/V emerge as promising candidates based on formation energies, high interface strengths, and favorable elastic contrasts. Focusing on TiN/Nb—due to superior oxidation resistance—we fabricate multilayers via non-reactive sputtering and confirm the formation of distinct TiN and Nb layers. Compression tests on FIB-milled micropillars reveal that the deformation behavior is governed by bilayer period (Λ) and TiN:Nb layer-thickness ratio (Γ). Systems with lower Γ exhibit increased compressive strain-to-failure, while those with higher TiN content (Γ = 6) show a more brittle-like fracture. The observed plasticity aligns with confined layer slip (CLS) behavior, where dislocation motion is restricted to the metallic Nb layers. These findings demonstrate that TiN/Nb multilayers can be tailored for improved toughness and ductility, offering a pathway towards advanced coatings for extreme environments.

## 1. Introduction

The development of protective coatings through innovative alloying concepts and architectural design has been a central focus in materials science for decades. These coatings play a critical role in extending the service life and performance of high-stress components such as turbine blades, cutting tools, and pistons, with the overarching goals of enhancing hardness, wear resistance, and fracture toughness [1–3]. Among the most promising strategies, multilayer coatings—consisting of alternating layers of distinct materials—have demonstrated exceptional potential. By tailoring individual layer thicknesses and material combinations, multilayers enable the optimization of mechanical and thermal properties such as hardness, toughness, oxidation resistance, and crack deflection, which are often unattainable in single-phase systems [4–8].

Transition metal nitrides, carbides, and borides are particularly valued for their high hardness, thermal stability, and wear resistance, making them prime candidates for demanding applications. When combined with metallic layers in multilayer architectures, these ceramics offer new pathways for optimizing performance. Systems integrating nitrides or carbides (e.g., TiN, CrN) with metals (e.g., Ti, Cr, Cu, Al) leverage the individual strengths of each phase—yielding coatings with improved fracture toughness, ductility, and oxidation resistance beyond that of monolithic coatings [9–17]. Mechanical properties can be tuned via bilayer period (Λ) and individual layer thicknesses: ultrathin layers often increase hardness via the Hall–Petch or superlattice effect [5,18], while thicker metallic layers enhance ductility and inhibit crack propagation. The atomic structure and quality of interfaces further govern the mechanical response, as dislocation motion and bonding strength across layer boundaries critically affect both strength and deformability.

Despite these advantages, combinations of nitrides or carbides with high-temperature metals remain comparatively underexplored [15–17,19–21]. This is especially true for multilayers involving group V and VI refractory metals, which offer excellent thermal and mechanical properties. One major challenge is the deposition of such materials

* Corresponding author at: Institute of Materials Science and Technology, TU Wien, Getreidemarkt 9, 1060 Wien, Austria.
*E-mail address:* paul.mayrhofer@tuwien.ac.at (P.H. Mayrhofer).

https://doi.org/10.1016/j.matdes.2025.114272
Received 14 April 2025; Received in revised form 27 May 2025; Accepted 18 June 2025
Available online 21 June 2025

under reactive environments, where strong nitride or carbide formers can lead to gas intermixing and degradation of metallic layers. Using composite ceramic targets for physical vapor deposition (PVD) in inert atmospheres offers a promising route to overcome this issue, as it suppresses gas-phase cross-contamination and ensures clean interface formation [22].

Selecting optimal ceramic–metal pairings remains a key challenge in designing high-performance multilayers. Recent advances in high-throughput modeling and density functional theory (DFT) enable systematic screening of candidate materials by predicting their thermodynamic stability, elastic behavior, and interface energetics [23–25]. When combined with micromechanical testing techniques, such as focused ion beam (FIB) milled micropillar compression, this approach allows for direct correlation between atomic-scale predictions and deformation behavior at the submicron level [26–29]. These tests can elucidate the dominant deformation mechanisms—such as confined layer slip, grain boundary activity, and shear localization—guiding the development of coatings with tailored mechanical performance [30].

In this study, we investigate 30 ceramic–metal multilayer combinations based on group IV transition metal nitrides or carbides (XN/XC, X = Ti, Zr, Hf) with high-temperature metals (M = V, Nb, Ta, Mo, W), using DFT to evaluate formation energies, interface strength, and elastic properties. TiN/Nb and TiN/V multilayers emerge as the most promising systems. Due to its superior oxidation resistance, TiN/Nb is selected for experimental validation via non-reactive PVD. We systematically vary the bilayer period ($\Lambda$) and TiN:Nb thickness ratio ($\Gamma$) and study the deformation mechanisms using micropillar compression. Our results reveal that both parameters significantly influence plasticity and failure behavior, with trends that are consistent with confined layer slip within the Nb layers. These findings provide a foundation for designing tough, ductile ceramic–metal multilayers for extreme environments.

## 2. Methodology

DFT calculations on XN/M and XC/M [nitrides (XN) or carbides (XC) of the group IV transition metals, X = {Ti, Zr, Hf}, with the group V–VI high-temperature metals, M = {V, Nb, Ta, Mo, W}] multilayer structures were performed using the Vienna Ab initio Simulation Package (VASP) [31,32] together with plane-wave projector augmented wave (PAW) pseudopotentials [33] and the Perdew-Burke-Ernzerhof generalized gradient approximation (GGA) [34]. The plane-wave cutoff energy of 600 eV and the reciprocal space sampling with Γ-centered Monkhorst-Pack meshes [35] ensured a total energy accuracy of at least $10^{-3}$ eV/at. Equilibrium lattice constants of these multilayer building components were evaluated by fitting the energy vs. volume curve, while the interfaces were fully optimized by relaxing their volume, cell shape, and atomic positions. Relative chemical stability was estimated by calculating formation energy, $E_f$ (Eq. (1) in Ref. [23]), while mechanical stability [36] and elastic moduli were assessed from the elastic constants, calculated using the stress–strain approach [37,38]. Interface strength was estimated by calculating cleavage energy, $E_{cl}$, and cleavage stress, $\sigma_{cl}$, according to Refs. [39,40]. The calculated Young's modulus $E$ of isotropic polycrystalline aggregates are obtained by Hill's [41] averages.

Based on these DFT considerations, various TiN/Nb multilayer coatings were non-reactively sputtered using an AJA Orion 5 system equipped with a three-inch ceramic TiN target and a two-inch metallic Nb target (both from Plansee Composite Materials GmbH, 99.5 % purity). The deposition chamber was evacuated to a base pressure of $\leq 0.1 \times 10^{-3}$ Pa before being filled with high-purity Ar (99.999 %). The substrates, mounted on a rotatable holder (1 Hz rotation), were heated to $T_s = 420$ °C. Prior to deposition, they were Ar-ion-etched for 10 min at a total pressure of 6 Pa with a DC etching potential of –500 V.

For the deposition of the TiN/Nb multilayers, the Ar flow was reduced to 10 sccm, and the working gas pressure was maintained at 0.4 Pa using a Baratron gauge. The substrates were biased with a DC potential of $U_b = -80$ V, while the TiN target was powered at 1 A DC and the Nb target at 0.6 A DC. Single-side polished (1 $\bar{1}$ 02)-oriented sapphire platelets ($10 \times 10 \times 0.53$ mm$^3$) served as substrates. The confocal-aligned cathodes were positioned 110 mm from the substrate holder.

Three series of multilayers with varying TiN:Nb layer-thickness ratios ($\Gamma = \ell_{TiN}:\ell_{Nb}$) of 1:1, 3:1, and 6:1 were prepared, each featuring three different bilayer periods ($\Lambda = \ell_{TiN}+\ell_{Nb}$) of 50, 100, and 450 nm. This resulted in 3 × 3 different multilayers containing 50, 25, and 5 bilayers, respectively, with a total thickness of 2.1–2.8 μm. These desired architectures were achieved using computer-controlled shutters positioned above the TiN and Nb targets. During deposition, the shutters were alternately opened for specific time intervals, while the cathodes remained continuously powered behind closed shutters, to precisely control the individual layer thicknesses. The shutter timing was calibrated based on pre-studies of monolithic TiN and Nb films to account for their respective deposition rates.

Structural analysis was performed using X-ray diffraction (XRD) on a Panalytical X'Pert II θ-θ diffractometer equipped with a Cu-Kα source in Bragg-Brentano geometry. The recorded diffraction patterns were analyzed using the HighScore Plus software.

For mechanical testing, micropillars with diameters of 485 ± 14 nm, 875 ± 30 nm, and 1250 ± 6 nm, all featuring a shank-angle of 2.3 ± 0.4°, were fabricated from six multilayers via focused ion beam (FIB) milling using an FEI Quanta™ 3D FEG FIB-SEM. Each pillar geometry was prepared in triplicate, resulting in three measurements per geometry. Thus, in total, 54 pillars (6 × 3 × 3) were tested. The pillars were aligned along the growth direction (perpendicular to the layer interfaces) and had a height of 2.1–2.8 μm, corresponding to the total multilayer thickness. Milling was carefully stopped at the coating-substrate interface. Coarse FIB milling was conducted at 7 nA, followed by finishing steps at 50 pA to minimize Ga ion damage.

The micropillars were compressed in-situ using a FemtoTools FT-NMT04 nanoindenter, equipped with a 5 μm flat punch diamond tip, inside an FEI Quanta 250 FEG-SEM. The system, capable of applying up to 200 mN, maintained a noise level below 5 μN (measured at 10 Hz). Compression tests were conducted at room temperature in displacement-controlled mode with a displacement rate of 5 nm/s. The engineering stresses and strains were calculated following the approach in [42].

Selected deformed pillars were further analyzed via transmission electron microscopy (TEM) using an FEI TECNAI F20 operated at 200 kV. Following initial compression, site-specific TEM lamellae were prepared from the micropillars using an FEI Scios™ 2 DualBeam™ FIB/SEM. A protective tungsten cap layer was first deposited to preserve the surface structure. The exposed sides were then shaped using a 500 pA $Ga^+$ ion beam to define the lamella geometry. Material removal from the base and sidewalls enabled lift-out of the lamella, which was subsequently attached to a copper TEM grid. Final polishing was carried out at a stage tilt of ±2°, using a reduced ion beam current of 50 pA to achieve electron transparency and minimize ion-induced damage—a corresponding procedure was used for non-deformed material). TEM analyses, including Fast Fourier Transform (FFT) evaluations, were performed using the Gatan Digital Micrograph 3 software package.

## 3. Results and discussion

### 3.1. Material selection based on ab initio screening

To identify the most promising material combinations for experiments, 30 multilayered systems were investigated with DFT calculations. These XN/M and XC/M multilayers combined nitrides (XN) or carbides (XC) of the group IV transition metals, X = {Ti, Zr, Hf}, with the group V–VI high-temperature metals, M = {V, Nb, Ta, Mo, W}. While the nitrides and carbides preferentially crystallize in the face-centered cubic (fcc) lattice, the metals adopt the body-centered cubic (bcc) structure.

To form (semi-)coherent interfaces, the bcc lattice must be rotated by 45° with respect to the fcc, i.e. $[1\,0\,0]_{fcc} \parallel [1\,1\,0]_{bcc}$. We selected material combinations based on their thermodynamic and mechanical stability, indicated by negative formation energy values ($E_f$, Fig. 1a) and elastic stability criteria.

Additionally, we considered their tendency to form sharp interfaces without intermixing ($\Delta E_f$, Fig. 1b), high interface strength (quantified by the difference in cleavage energy between the multilayer stack and the parent ceramic component $\Delta E_{cl}$, Fig. 1c), and significant differences in elastic moduli of the multilayer components ($\Delta E$, Fig. 1d). Thus, $E_f$ should be highly negative, $\Delta E_f$, should be minimally negative or even positive, $\Delta E_{cl}$ should be large, and $\Delta E$ between the ceramic and metal should be high. Large differences in elastic moduli of the multilayer building blocks lead to variations of the stress/strain fields at the interfaces [5,43,44], which help dissipate energy during crack propagation, especially when major propagation direction is perpendicular to the interfaces.

Although no formal weighting scheme was applied to the selection criteria, priority was given to identifying combinations with low formation energies and strong interfacial bonding, as these indicate favorable thermodynamic stability. Differences in elastic moduli between the ceramic and metallic components were considered a secondary factor, potentially influencing stress partitioning at the interface, but not used as a primary design parameter. For instance, TiN exhibits a high polycrystalline Young's modulus (~450 GPa) and a directional modulus along ⟨100⟩ (~520 GPa), whereas bcc-V (70.9 GPa) and bcc-Nb (83.6 GPa) are significantly more compliant. These pairings result in pronounced modulus mismatches ($\Delta E$) for the TiN/V and TiN/Nb systems (Fig. 1d), which may influence local mechanical response.

In terms of thermodynamic stability, the TiN/V and TiN/Nb interfaces exhibit low formation energies ($E_f$, Fig. 1a), and among the evaluated XN/M combinations, they also show the least negative differences in $E_f$ (Fig. 1b). Moreover, both systems display relatively high interface strength, as approximated by the cleavage energy difference between the multilayer stack and the parent ceramic component (Fig. 1c). While TiN/V offers a slightly less negative $\Delta E_f$, TiN/Nb provides a higher interfacial bonding energy ($\Delta E_{cl}$), suggesting stronger interfacial cohesion. Additionally, Nb provides superior oxidation resistance compared to V. Based on these combined considerations—thermodynamic favorability, interfacial strength, and environmental stability—the TiN/Nb system was selected for experimental investigation.

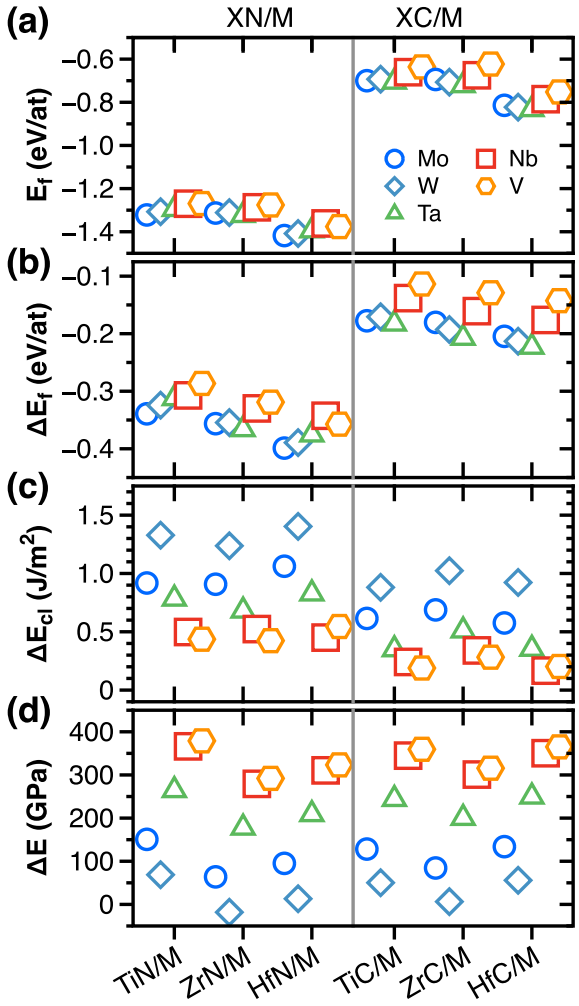


**Fig. 1.** Ab initio screening of XN/M and XC/M multilayered systems and their fcc-XN, fcc-XC, and bcc-M components, where X = {Ti, Zr, Hf}, M = {V, Nb, Ta, Mo, W}. Formation energy $E_f$ of the multilayer **(a)**, difference between the multilayer and its constituent components (fcc-XN, fcc-XC, and bcc-M) of their formation energy $\Delta E_f$ **(b)**, cleavage energy $\Delta E_{cl}$ **(c)**, and polycrystalline Young's moduli $\Delta E$ **(d)**.

### 3.2. Thin film deposition

Titanium and niobium both have a strong tendency to form nitrides, as confirmed by DFT calculations predicting energy of formations $E_f$ of −1.966 eV/at for TiN [45] and −0.998 eV/at for NbN [23,45,46]. Therefore, we selected a non-reactive deposition route, sputtering TiN layers from a ceramic TiN target and metallic Nb layers from an Nb target. This approach ensures that the chamber remains nitrogen-free during the Nb layer deposition. To enhance coating–substrate adhesion, the first layer was always Nb. As described in the methodology section, we prepared three series of multilayers, classified by their layer-thickness ratio $\Gamma = \ell_{TiN}{:}\ell_{Nb} = 1$, 3, and 6. Within each series we aimed for bilayer periods of $\Lambda = 50$, 100, and 450 nm. Cross-sectional SEM and TEM analyses confirm that the individual layer-thickness ratios were achieved, while the bilayer periods slightly deviate from the target values. The measured bilayer periods fall within $\Lambda = 51 \pm 4$ nm, $96 \pm 17$ nm, and $420 \pm 11$ nm. For accuracy, we refer to each of the nine distinct multilayers by its specific Γ–Λ combination: 1–420 nm, 1–108 nm, 1–55 nm, 3–420 nm, 3–84 nm, 3–51 nm, 6–420 nm, 6–100 nm, and 6–48 nm, with individual layer thicknesses determined by:

$$\ell_{Nb} = \frac{\Lambda}{\Gamma + 1}$$

$$\ell_{TiN} = \Lambda - \frac{\Lambda}{\Gamma + 1} = \frac{\Lambda \cdot \Gamma}{\Gamma + 1} \quad (1)$$

In addition, cross-sectional TEM investigations further confirm the excellent semi-coherent growth of the two layers, TiN and Nb. This is exemplified in Fig. 2a, b and c, which present the multilayer with $\Gamma = 1$ and $\Lambda = 55$ nm, and in Fig. 2d, e, and f, which show the multilayer with $\Gamma = 1$ and $\Lambda = 420$ nm.

The lower-magnification TEM images (Fig. 2a, b, d, and e) reveal that the individual TiN and Nb layers follow the crystallographic orientation of the underlying grains, resulting in a columnar-like growth morphology. This feature is evident in both multilayers with bilayer periods of 55 nm and 420 nm. The grain sizes appear consistent across both samples, with their length constrained by the respective layer thicknesses and widths ranging from 30 to 40 nm—significantly smaller than the diameter of even the smallest compression pillars. High-resolution TEM (HR-TEM) images (Fig. 2c and f) further confirm the semi-coherent growth of TiN and Nb at the interfaces.

The phase identity and crystal structures were validated by selected area electron diffraction (SAED) patterns obtained from multilayers with $\Gamma = 1$ and $\Lambda = 55$ nm (Fig. 2a3) and 420 nm (Fig. 2d3). For the 55 nm period, the SAED aperture encompassed several TiN and Nb layers,

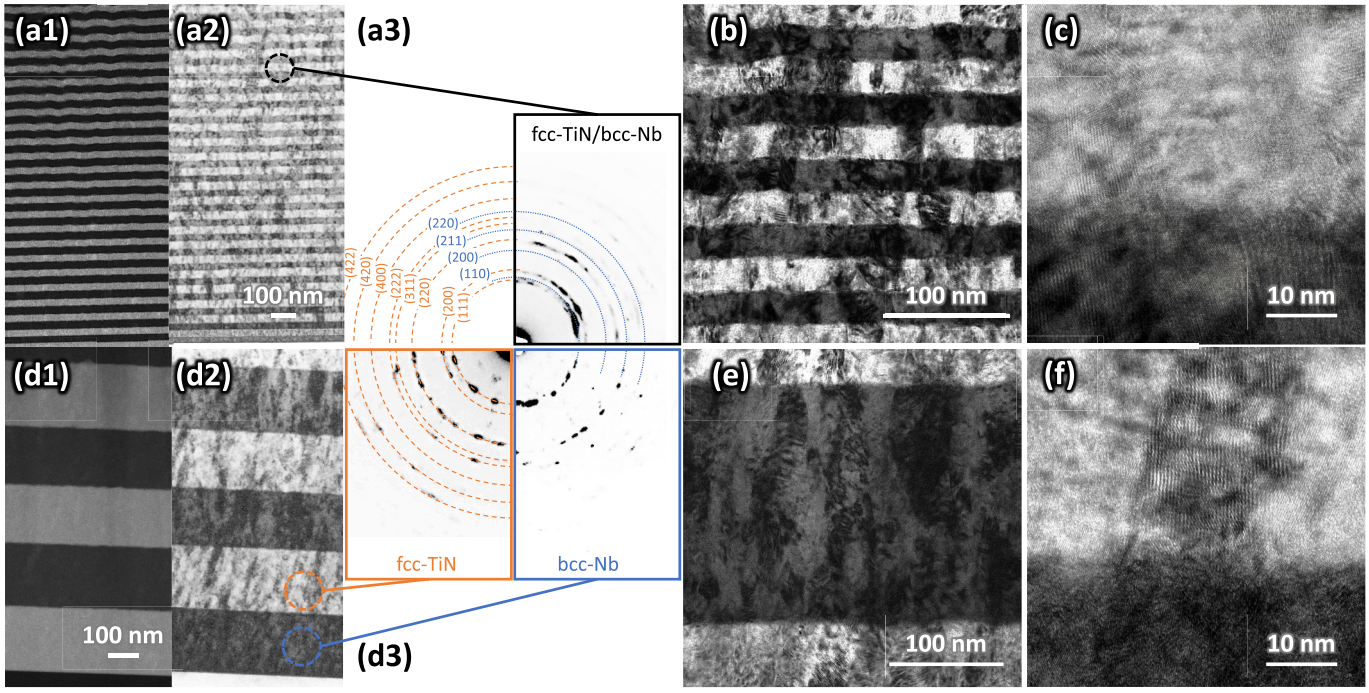


**Fig. 2.** Cross-sectional TEM images of TiN/Nb multilayers, illustrating their microstructure and semi-coherent growth. **(a1)** HAADF-STEM (mass contrast) and **(a2)** bright-field TEM image of a multilayer with $\Gamma = 1$ and $\Lambda = 55$ nm, showing well-defined, alternating TiN and Nb layers. **(a3)** SAED pattern acquired from the region marked in **(a2)**, covering both TiN and Nb layers; diffraction rings correspond to fcc-TiN (indexed with rusty dashed circle segments) and bcc-Nb (indexed with bluish solid circle segments). **(b)** Medium-magnification and **(c)** high-resolution TEM images of a TiN/Nb interface within the $\Lambda = 55$ nm multilayer. **(d1)** HAADF-STEM and **(d2)** bright-field TEM images of a multilayer with $\Gamma = 1$ and $\Lambda = 420$ nm, revealing thicker individual layers. **(d3)** SAED pattern showing isolated diffraction from individual layers (region of investigation marked in **(a2)**), with fcc-TiN and bcc-Nb clearly resolved. **(e)** Medium-magnification and **(f)** high-resolution TEM images of the TiN/Nb interface in the $\Lambda = 420$ nm multilayer. Scale bars are identical in **(b)**/**(e)** and **(c)**/**(f)**. In bright-field images, Nb appears darker and TiN brighter due to differences in electron scattering, whereas in HAADF-STEM images (**a1, d1**), the heavier Nb appears brighter and the lighter TiN darker.

resulting in a diffraction pattern that clearly exhibits contributions from both fcc-TiN and bcc-Nb phases (Fig. 2a3). In contrast, the larger bilayer period of 420 nm enabled individual SAED measurements of TiN and Nb layers, unambiguously confirming their respective fcc and bcc crystal structures (Fig. 2d3).

### 3.3. Structural analysis

The comparison of the XRD patterns, Fig. 3, shows that all multilayers exhibit a mixed polycrystalline growth orientation. Within each series with $\Gamma = 1$ (Fig. 3a) or 3 (Fig. 3b) or 6 (Fig. 3c), peak profile widths

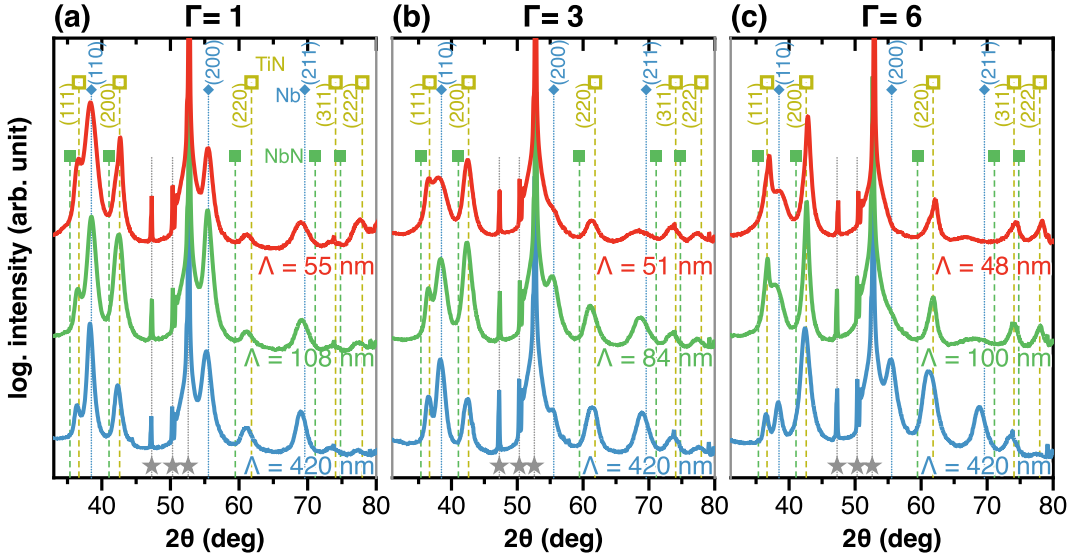


**Fig. 3.** XRD patterns of the three TiN/Nb multilayer series with layer ratios $\Gamma = 1$ **(a)**, $\Gamma = 3$ **(b)**, $\Gamma = 6$ **(c)**. Each series contains three distinct bilayer periods, with the individual patterns labeled by their corresponding $\Lambda$. The standard positions for bcc-Nb (#00–035-0789) are marked with bluish full rhombus symbols, those of fcc-TiN (#00–038-1420) with yellowish empty cubes, those of fcc-NbN (#03–065-2877) with green full cubes (exemplarily labeled in **(a)**), and those of the sapphire substrate with a star symbol. XRD data are plotted on a logarithmic scale to highlight weaker peaks. Reflections correspond to TiN and Nb, indicating phase-pure, textured layers. (For interpretation of the references to colour in this figure legend, the reader is referred to the web version of this article.)

increase as Λ decreases, indicating smaller coherently diffracting domain sizes and increasing microstresses. As the layer-thickness ratio Γ increases (Fig. 3a to b), the contribution of TiN becomes more pronounced. However, Nb remains detectable even for the highest Γ of 6 combined with the smallest Λ of 48 nm. At this point, the Nb layer is thinnest with around 7 nm. There is no indication of fcc-NbN phase formation, even for the lowest Γ of 1 combined with the largest Λ of 420 nm, where the Nb layer is thickest with around 210 nm. Together with the TEM and SAED investigations this confirms the successful separated formation of nitride and metal layers, as intended by the non-reactive deposition route.

### 3.4. Fracture stress and appearance

The individual multilayers were tested for their resistance to compression by recording the force and calculating the engineering stress (σ) during micro-compression tests of FIB-machined pillars. The pillars were extracted from the multilayers with their axis aligned along the coating growth direction, meaning the multilayers were loaded perpendicular to the TiN/Nb interfaces (see the methodology section for more details).

For six multilayers, three different pillar diameters were prepared. To ensure statistical reliability, each geometry was fabricated and tested three times, resulting in a total of nine tests per multilayer. Fig. 4 presents the obtained stress–strain (σ–ε) curves during pillar compression. The most characteristic multilayers are tested, illustrating the effect of decreasing the bilayer period Λ and increasing Γ. Specifically, for the smallest Γ of 1, Λ is reduced from 420 nm (Fig. 4a) to 108 nm (Fig. 4b) to 55 nm (Fig. 4c). For the intermediate Γ of 3, Λ decreases from 84 nm (Fig. 4d) to 51 nm (Fig. 4e). Finally, the largest Γ of 6 is combined with the smallest Λ of 48 nm (Fig. 4f), thus for a bilayer period of Λ ~ 50 nm, Γ is increased from 1 to 3 to 6. Important to mention is that the two Γ–Λ combinations 1–55 nm (Fig. 4c) and 3–108 nm (Fig. 4d) hold a very similar Nb-layer thickness of $\ell_{Nb}$ = 27.5 and 21 nm, respectively (cf. with Eq. (1)).

The initial compressive yield strength $R_{p0.2}$ was determined as the stress corresponding to a plastic strain $\varepsilon_p$ = 0.2 %. This value was obtained by constructing a 0.2 % offset line, which intersects the measured σ–ε curve. The slope of this offset line was derived from a linear fit of the initial elastic region of the σ–ε curve to ensure an accurate representation of the material's elastic response, as exemplified in Fig. 4a. For samples that fractured without noticeable plastic deformation, we also used $R_{p0.2}$ for the fracture stress to maintain consistency and avoid confusion due to multiple symbols.

Samples exhibiting increased ductility accommodate greater overall compression (%) before complete failure, often corresponding to lower maximum engineering stresses. Additionally, ductile samples retain some resistance to deformation even after crack initiation, whereas less ductile samples experience a more abrupt drop in engineering stress. Consequently, pillars exhibiting a more brittle response show a sharp drop in engineering stress once the maximum compressive load is exceeded—most notably in the multilayer with Γ = 6 and Λ = 48 nm (Fig. 4f). This configuration, with the highest TiN fraction and thinnest Nb layers (~7 nm), demonstrates the lowest compressive strain-to-

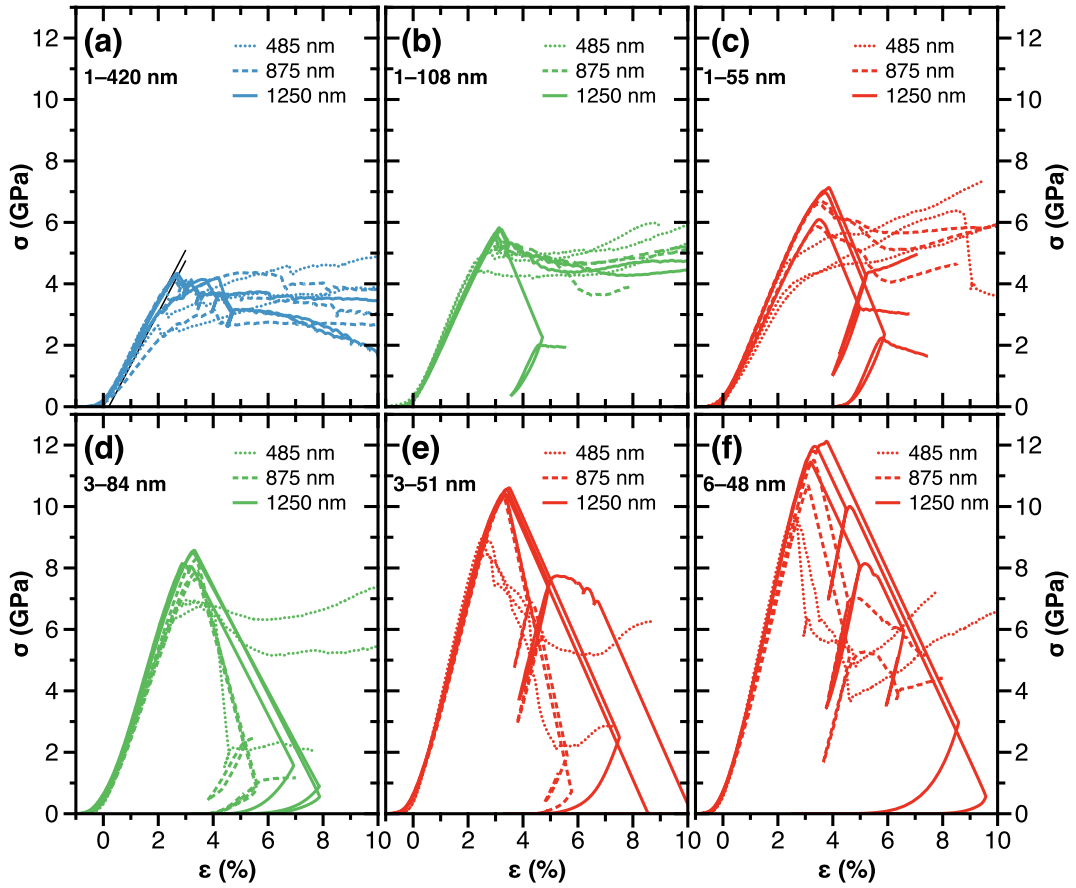


**Fig. 4.** Engineering stress σ during compression of micropillars of the TiN/Nb multilayers with the Γ–Λ combination of 1–420 nm **(a)**, 1–108 nm **(b)**, 1–55 nm **(c)**, 3–84 nm **(d)**, 3–51 nm **(e)**, and 6–48 nm **(f)**. The σ–ε curves of pillars with 485 nm, 875 nm, and 1250 nm diameter are displayed as dotted, dashed, and solid lines, respectively. The $R_{p0.2}$ values—obtained by constructing a 0.2 % offset line to the linear fit of the initial elastic region of the σ–ε curve, schematically shown in **(a)**—of the 1250-nm-diameter pillars are 4.19 ± 0.13, 5.71 ± 0.07, 6.47 ± 0.34, 8.25 ± 0.20, 9.99 ± 0.07, and 11.66 ± 0.26 GPa for the 1–420 nm **(a)**, 1–108 nm **(b)**, 1–55 nm **(c)**, 3–84 nm **(d)**, 3–51 nm **(e)**, and 6–48 nm **(f)** specimens.

failure. As the TiN fraction decreases (Γ decreasing from 6 to 3 to 1), the pillars display progressively more ductile behavior (see Fig. 4f, 4e, and 4c). We attribute the limited plasticity at high TiN content to dislocation motion being increasingly hindered by the interfaces and the reduced volume fraction of ductile Nb.

Furthermore, within a given Γ, ductility increases with increasing bilayer period Λ, corresponding to an increase in Nb layer thickness (compare Fig. 4e and 4d for Γ = 3, and Fig. 4c, 4b, and 4a for Γ = 1). The highest ductility is observed in the TiN/Nb multilayer with Γ = 1 and the thickest Nb layers ($\ell_{Nb}$ = 210 nm for Λ = 420 nm), as shown in Fig. 4a. Across all pillar diameters, no fully brittle failure was observed. A similar trend is found for the TiN/Nb multilayer with Γ = 1 and Λ = 108 nm ($\ell_{Nb}$ = 54 nm), where only one pillar (with the largest diameter of 1250 nm) fractured in a predominantly brittle manner (Fig. 4b). For the TiN/Nb multilayer with Γ = 1 and Λ = 55 nm ($\ell_{Nb}$ = 27.5 nm), all three 1250-nm-diameter pillars exhibited failure that was essentially brittle (Fig. 4c). Most of the pillars—particularly those with smaller diameters—exhibit a more apparent strain hardening, which is primarily attributed to the Nb layers.

As expected, the yield strength $R_{p0.2}$ of this Γ = 1 series increases with decreasing Λ, from ~4.2 GPa (Λ = 420 nm) to ~5.7 GPa (Λ = 108 nm) to ~6.7 GPa (Λ = 55 nm), when comparing the thickest pillars with 1250 nm diameter. However, these bilayer period variations are well above the range where a superlattice effect would be expected. Thus, the increasing $R_{p0.2}$ primarily results from changes in the thin Nb layers, whose thicknesses accordingly decrease from $\ell_{Nb}$ = 210 nm to 54 nm to 27.5 nm. A similar trend is observed for the Γ = 3 multilayers, but due to the higher TiN fraction, failure becomes increasingly abrupt in the 875-nm-diameter pillars for Λ = 84 nm (Fig. 4d), while only one of the smallest-diameter pillars exhibits noticeable plastic deformation for Λ = 51 nm (Fig. 4e). Here, $R_{p0.2}$ also increases with decreasing Λ, from ~8.3 GPa (Λ = 84 nm) to ~10.0 GPa (Λ = 51 nm), as the Nb-layer thickness decreases from $\ell_{Nb}$ = 21 nm to 13 nm, for the thickest pillars of 1250 nm diameter.

The TiN/Nb multilayer with the highest TiN fraction (Γ = 6) exhibits minimal plasticity, particularly for the smallest Λ of 48 nm, which contains the thinnest Nb layer among all multilayers studied ($\ell_{Nb}$ = 7 nm), Fig. 4f. The $R_{p0.2}$ for this TiN/Nb multilayer—obtained from the 1250-nm-diameter pillar—can be estimated to ~11.7 GPa.

This comparison highlights that deformation behavior is influenced not only by the multilayer structure (layer-thickness ratio, Γ = $\ell_{TiN}$:$\ell_{Nb}$, and bilayer period, Λ) but also by pillar diameter. For example, the multilayer with Γ = 1 and Λ = 55 nm exhibits compressive strain-to-failure for 485-nm- and 875-nm-diameter pillars, whereas the larger ones display predominantly brittle characteristics (Fig. 4c). However, the σ–ε curves for the two larger-diameter pillars are generally more consistent, and the obtained $R_{p0.2}$ are closer to each other compared to those obtained from the 485-nm-diameter pillar. Correspondingly, the multilayer with Γ = 3 and Λ = 84 nm deforms plastically in the 485-nm-diameter pillars but exhibits more abrupt failure in the 875-nm- and 1250-nm-diameter pillars.

The unexpected increase in yield strength for 1250-nm-diameter pillars compared to 485-nm-diameter pillars—unexpected, because typically smaller is stronger [26,47]—can be attributed to several microstructural and deformation-related factors. While all pillars are polycrystalline with grain sizes much smaller than their diameters, the 485-nm-diameter pillar appears to transition into a different deformation regime. Its lower yield strength suggests that grain boundary-mediated deformation mechanisms, such as grain boundary sliding and rotation, play a more dominant role, facilitating earlier plasticity. In contrast, the 875-nm- and 1250-nm-diameter pillars exhibit similar mechanical behavior, indicating that their deformation is governed more by dislocation interactions and storage, leading to higher yield strength. Furthermore, the 485-nm-diameter pillar shows increased plasticity and a higher strain hardening rate, likely due to enhanced dislocation-grain boundary interactions and the activation of geometrically necessary dislocations. Additionally, FIB-induced defects may have a stronger relative influence on the 485-nm-diamter pillar, further lowering its initial strength while promoting more extended plastic deformation. The similarity in behavior between the 875-nm-diamter and 1250-nm-diamter pillars suggests that a critical pillar size exists above which the mechanical response stabilizes, making the 485-nm-diamter pillar more prone for small-scale effects.

However, all multilayers with Γ = 1 and 3 (even those with the smallest Λ) show at least some plastic deformation in their stress–strain curves for the smallest-diameter pillars (Fig. 4b–e), indicating that ductility is present even when the overall response suggests a more brittle nature. The multilayers with Γ = 6 combined with the smallest Λ = 48 nm (containing the thinnest Nb layers among all multilayers studied with $\ell_{Nb}$ = 7 nm) also exhibit noticeable plasticity—specifically for the thinnest diameter pillar—though to a lesser extent than the Γ = 3 counterparts. Due to the thinner Nb layers, the yield strength is significantly higher, which likely contributes to the more abrupt failure characteristics.

SEM investigations of the tested pillars reveal that failure in the more brittle-responding multilayers is characterized by shearing along a fracture plane with limited observable plastic deformation in the Nb layers. In contrast, more compressive strain-to-failure behavior is evident when clear signs of plastic deformation appear in the Nb layers. This plasticity is observed in the pillars of multilayers with the Γ–Λ combinations of 1–420 nm (Fig. 5a), 1–108 nm (Fig. 5b), 1–55 nm (Fig. 5c), 3–84 nm (Fig. 5d), and 3–51 nm (Fig. 5e). The multilayer with Γ = 6 (highest TiN fraction) and the thinnest Nb layers ($\ell_{Nb}$ = 7 nm for Λ = 48 nm) also shows some plastic deformation, though less pronounced than in the Γ = 3 multilayers, before ultimately failing at a high yield strength (compare Fig. 4f and 5f).

### 3.5. Confined layer slip model

Analyzing the $R_{p0.2}$ data obtained from compression tests of the various TiN/Nb multilayers for their dependence on specific multilayer characteristics—such as bilayer period (Λ), layer-thickness ratio (Γ), or Nb layer thickness ($\ell_{Nb}$)—does not reveal a clear correlation, see Fig. 6a, b, and c, respectively. In analogy to the Hall–Petch relation, we plotted $R_{p0.2}$ against the inverse square roots of Λ and $\ell_{Nb}$. Additionally, comparing $R_{p0.2}$ values of the multilayers with the mean $R_{p0.2}$ of Nb and TiN does not provide a clear correlation either; instead, the overall trend is similar to that of $R_{p0.2}$ vs. Γ (Fig. 6b). As a reference value for TiN, we used an $R_{p0.2}$ estimate derived from nanoindentation hardness via the Tabor relation ($H \approx C \cdot R_{p0.2}$) [48], with $C \approx 2.4$ for TiN-like coatings, as discussed in Ref. [18] when reviewing the Tabor relation. For a non-reactively prepared TiN coating—identical to that used in the TiN/Nb multilayers—we calculated $R_{p0.2}$ from its hardness of 29.5 ± 1.9 GPa [22], yielding ≈ 12.3 ± 0.8 GPa. This estimate aligns well with the 14 GPa yield-strength obtained from micro-compression tests of Ti(C,N) and Zr(C,N) coatings [49]. The $R_{p0.2}$ of Nb is ~ 0.059 GPa [50], increasing to ~0.95 GPa when heavily deformed, as inferred from the diagram in [51].

While Fig. 6 indicates that $R_{p0.2}$ generally increases with decreasing Λ or increasing layer-thickness ratio (Γ), it does not account for variations in $R_{p0.2}$ observed in multilayers with the same Λ or Γ values. The strongest correlation of this comparison is found when plotting $R_{p0.2}$ against the Nb layer thickness $\ell_{Nb}$ (Fig. 6c), highlighting the significant influence of the Nb layers on $R_{p0.2}$. However, even in this case, the two multilayers with very similar Nb layer thicknesses ($\ell_{Nb}$ = 27.5 nm and 21 nm) but different Γ–Λ combinations (1–55 nm and 3–84 nm) are not considered independently, suggesting additional factors at play.

Similar trends have been observed in other ceramic/metal multilayers, such as TiN/Cu and $Al_2O_3$/Nb, where the strength increase is primarily controlled by interface-dominated mechanisms rather than bulk properties alone [15,16]. In these systems, confined layer slip (CLS) plays a key role in restricting dislocation motion and enhancing

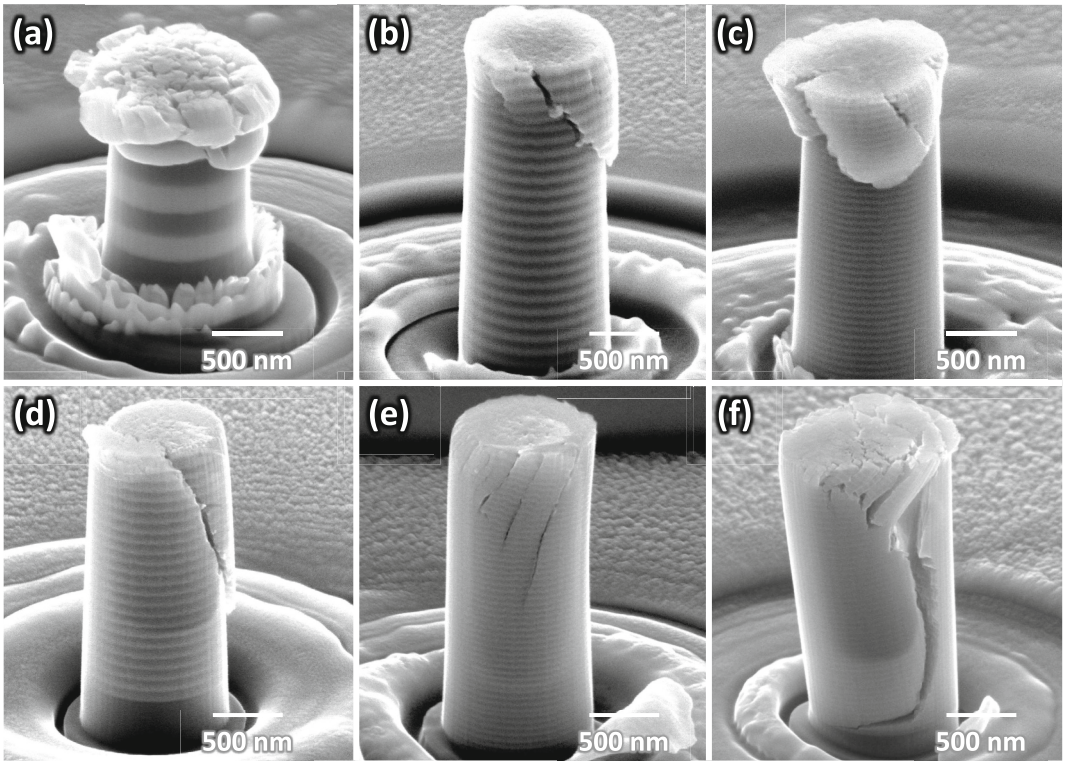


**Fig. 5.** SEM investigations of the tested 875-nm-diameter micropillars of the TiN/Nb multilayers with the Γ–Λ combination of 1–420 nm **(a)**, 1–108 nm **(b)**, 1–55 nm **(c)**, 3–84 nm **(d)**, 3–51 nm **(e)**, and 6–48 nm **(f)**. As indicated by the σ–ε curves, the multilayer with the highest TiN fraction (Γ = 6) combined with the thinnest Nb layer (Λ = 50 mm) exhibits the most brittle failure. The brighter layers represent Nb.

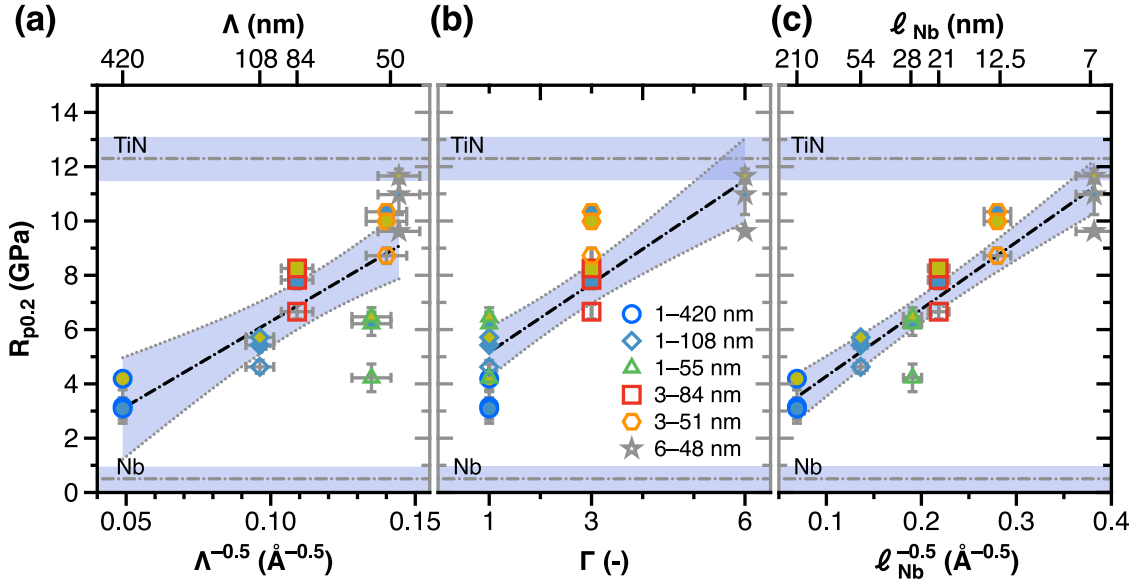


**Fig. 6.** Dependence of $R_{p0.2}$ of the TiN/Nb multilayers on their characteristics: bilayer period Λ **(a)**, layer-thickness ratio Γ **(b)**, and Nb-layer-thickness $\ell_{Nb}$ **(c)**. In analogy to the Hall–Petch relation, the plot against Λ and $\ell_{Nb}$ uses their inverse square roots. The individual data points are labeled by Γ–Λ of the respective multilayer. The smallest-diameter pillar is represented by not-filled symbols and the largest by yellowish filled ones. The dash-dotted horizonal grey lines represent the failure stress of TiN (12.3 ± 0.8 GPa) and $R_{p0.2}$ of Nb (0.059–0.95 GPa). The individual dash-dotted black lines correspond to linear fits with respect to the variables $\Lambda^{-0.5}$, Γ, or $\ell_{Nb}^{-0.5}$, including a 95 % confidence band.

strengthening effects as the metallic layer thickness decreases.

To further understand these trends, we also considered the confined layer slip (CLS) model for the metallic layer (Nb). This model, further developed by Nix [52], describes deformation in multilayer systems where dislocation motion is constrained within individual layers. When the layer thickness decreases below a critical threshold, dislocations are unable to form extended pile-ups but may still bow out within the layer, resulting in increased strengthening.

In this scenario, dislocation bowing propagates through the layer, and dislocations accumulate as a stretch at the interface rather than transmitting across it [53–55]. Such dislocation confinement has been extensively discussed for nanoscale multilayers, where the interface

structure plays a crucial role in governing plasticity [15,16]. The transmittance across interfaces becomes particularly complex when combining metal layers with nitride layers, as nitrides exhibit different Burgers vectors (and values), elastic constants, and Peierls barriers [18]. These differences significantly influence dislocation interactions and mobility at the interface, further affecting the mechanical response of the multilayer system. As a result, the yield strength increases inversely with the layer thickness, following a Hall–Petch-like relationship. This mechanism explains why $R_{p0.2}$ rises significantly as $\ell_{Nb}$ decreases, particularly in the thinnest Nb layers, where dislocation glide becomes increasingly confined. These results support the broader understanding that the mechanical performance of ceramic/metal multilayers is largely dictated by interfacial effects rather than bulk strengthening alone [15,16]. As a result, optimizing layer thickness—particularly the metallic layer—is a key strategy for tailoring the mechanical properties of multilayers for high-strength applications.

According to this model, the upper limit is determined by the shear stress τ required to bow a screw dislocation with a radius $r$ (half of the Nb layer thickness $\ell_{Nb}$) on specific glide planes, given by the following expression [53]:

$$\tau = \frac{G \cdot b}{4 \cdot \pi \cdot r} \ln\left(\frac{R}{r_0}\right) \tag{2}$$

where $G$ is the shear modulus of Nb, $b$ is the Burgers vector of Nb for screw dislocations on these specific glide planes, $R$ denotes the radius of the investigated cylindrical volume, and $r_0$ is the core radius of the dislocation (being in the order of $b$). Rewriting Eq. (2) according to:

$$\tau = \frac{G \cdot b}{4 \cdot \pi \cdot r} \ln\left(\frac{R}{r_0}\right) = \frac{G \cdot b}{4 \cdot \pi} \frac{\ln\left(\frac{R}{r_0}\right)}{r} = A \frac{\ln\left(\frac{R}{r_0}\right)}{r} \tag{3}$$

allows for a linear-like expression, where the layer-arrangement-specific variables define the $x$-coordinate, while the slope $A$ contains only material-specific constants (here, $G$ and $b$). Therefore, if a plot of $R_{p0.2}$ against $\ln\left(\frac{R}{r_0}\right)/r$ exhibits a linear relationship, the CLS model is applicable to these materials.

Fig. 7 confirms a linear relationship between $R_{p0.2}$ and $\ln\left(\frac{R}{r_0}\right)/r$ for the TiN/Nb multilayers. The linear fit includes a 95 % confidence interval, within which most date points fall. With $r_0$ = 2.86 Å (Burgers vector for the primary slip system of Nb {110}⟨111⟩), the fit yields a slope of 32.4 ± 3.6 GPa·Å, and an $x$-intercept of –0.13 GPa·Å. The $R^2$ value of 0.83 confirms the robustness of the trend. Increasing $r_0$ to 10 Å raises the slope to 38.3 ± 4.3 GPa·Å, while maintaining the intercept and $R^2$ value. Notably, the larger-diameter pillars also better follow the trend given by Eq. (3) that accounts for diameter effects (as included in the term $\ln\left(\frac{R}{r_0}\right)/r$), whereas the smallest 485-nm-diameter pillar deviates more significantly. Using the Taylor relation ($R_{p0.2} \approx 3 \cdot \tau$) [18,56], the slope of the fit is converted to be $A$ = 11.3 ± 1.3 GPa·Å ($r_0$ = 2.86 Å) or 13.4 ± 1.5 GPa·Å ($r_0$ = 10 Å) for Eq. (3), which aligns well with the calculated values of $A$ = 8.6 GPa·Å, 12.2 GPa·Å, and 15.8 GPa·Å, when using a shear modulus of $G$ = 38 GPa [57] and Burgers vectors $b$ of 2.86 Å, 3.92 Å, and 4.47 Å for the primary {110}⟨111⟩, secondary {112}⟨111⟩, and less common {123}⟨111⟩ slip systems, respectively. These calculated $A$ values for Nb correspond to 25.9 GPa·Å, 36.7 GPa·Å, and 47.3 GPa·Å when plotted for $R_{p0.2}$, which are used to draw the corresponding slopes in Fig. 7, labeled according to these {110}⟨111⟩, {112}⟨111⟩, and {123}⟨111⟩ slip systems.

The comparison between the experimentally obtained and calculated $A$ values suggests that especially for the Γ = 6 combined with Λ = 50 nm multilayers (6–48 nm) the contribution from the less common {123}⟨111⟩ slip system is minimal, with a greater contribution from the primary {110}⟨111⟩ slip system. This is in agreement with the larger

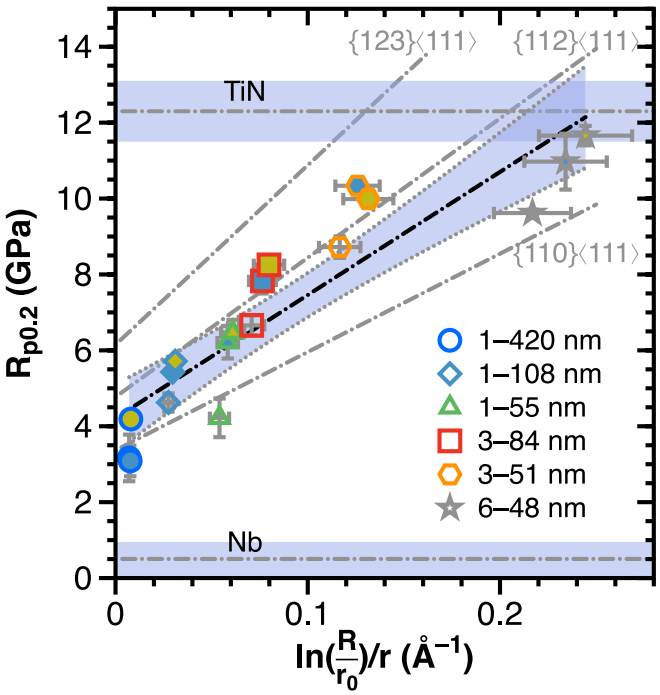


**Fig. 7.** Dependence of $R_{p0.2}$ on the factor $\ln\left(\frac{R}{r_0}\right)/r$—with R being the radius of the pillar (R = ½ of 485 ± 14 nm, 875 ± 30 nm, and 1250 ± 6 nm) from which $R_{p0.2}$ was obtained, r being ½ of the Nb-layer-thickness ($\ell_{Nb}$ obtained with Eq. (1) from Λ and Γ of the multilayers, see also Fig. 6), and $r_0$ = b = 2.86 Å for the dislocation core of the {110}⟨111⟩ primary slip system. The individual data points are labeled by Γ–Λ of the respective multilayer. The dash-dotted black line is a linear fit through all data. The dash-dotted horizonal grey lines represent the failure stress of TiN (12.3 ± 0.8 GPa) and $R_{p0.2}$ of Nb (0.059–0.95 GPa [50,51]). The smallest-diameter pillar is represented by not-filled symbols and the largest by yellowish filled ones. The three dash-dotted lines labeled {110}⟨111⟩, {112}⟨111⟩, and {123}⟨111⟩ represent slopes corresponding to the A values $A = \frac{G \cdot b}{4 \cdot \pi}$ from Eq. (3), considering the Taylor relation ($R_{p0.2} \approx 3 \cdot \tau$). These slopes reflect the different Burgers vectors b for each slip system. Variations in pillar diameter (R) and Nb-layer-thickness (r = ½·$\ell_{Nb}$) result in the error bar of the factor $\ln\left(\frac{R}{r_0}\right)/r$.

contribution from the (110) orientation in their Nb layers (see Fig. 3). For the multilayers with Γ = 1 and 3, the trend follows more closely the contributions of the secondary {112}⟨111⟩ slip system. Interestingly, both the 1–55 nm and 3–84 nm multilayers have a similar Nb-layer thickness and therefore their data are positioned close to each other in Fig. 7. The generally higher $R_{p0.2}$ values of the 3–84 nm multilayers can be attributed to their stronger (211) orientation of the Nb layers (Fig. 3b), whereas the 1–55 nm multilayers exhibit a more pronounced (110) orientation (Fig. 3a), which aligns with their lower $R_{p0.2}$ values and the different slopes of the CLS model.

However, for the multilayer with a higher TiN fraction (Γ = 6)—particularly when combined with the thinnest Nb layer (Λ = 48 nm, corresponding to $\ell_{Nb}$ = 7 nm)—the data appear to converge toward those of TiN itself, suggesting that the Nb layers contribute little, if at all, to the overall deformation behavior. This observation, along with the previously discussed σ–ε curves and SEM investigations of the tested pillars, suggests that significant plasticity is no longer present in these structures. These findings highlight that the compression deformation behavior of TiN/Nb multilayer coatings is governed by dislocation motion within the Nb layers down to a critical thickness $\ell_{Nb}$, below which plasticity is severely limited—especially when combined with a high TiN fraction, as observed for Γ = 6.

Since the TiN/Nb multilayers with symmetric bilayers (Γ = 1) exhibit significant plastic deformation across all bilayer periods (Figs. 4 and 5),

with a pronounced difference between $\Lambda = 420$ nm and 55 nm, these two samples were studied in more detail using TEM (Fig. 8). Due to its higher absorption coefficient, niobium appears darker, while TiN appears brighter in these TEM bright-field images. Fig. 8a provides an overview of the tested pillar of the multilayer with $\Lambda = 420$ nm, confirming that the bilayers are indeed symmetric, with a bilayer period of 420 nm—matching the values calculated from the individual deposition rates. A closer look at the marked region in Fig. 8a reveals a heavily deformed Nb layer, while the underlying TiN layer has cracked open, indicating a shear-deformation zone within Nb. This highlights the Nb layer's ability to plastically deform, whereas the TiN layer exhibits brittle failure.

The HR-TEM analysis of the transition region between the Nb and TiN layers (marked in Fig. 8b) shows that the TiN layer begins to fracture transcrystalline but predominantly follows an intercrystalline path, as seen in Fig. 8c in comparison to Fig. 8b. The corresponding FFT (inset of Fig. 8c) confirms that the transcrystalline fracture occurs along the (111) zone axis. Overall, these findings emphasize that the pronounced plastic deformation and shear capability of the 210-nm-thick Nb layer—enabled by substantial dislocation motion—effectively arrests cracks that form in the brittle TiN layer.

TEM studies of the multilayer with $\Lambda = 55$ nm confirm the symmetric bilayers, and similar to the multilayer with $\Lambda = 420$ nm, there is excellent agreement between the TEM measurements and values estimated from deposition rates, Fig. 8d. The σ–ε curve of this multilayer (Fig. 4c) suggests brittle failure in the 1250-nm-diameter pillar, which was also used for the TEM studies. However, although the TEM cross-section clearly reveals that the entire pillar sheared apart, the Nb layers clearly show plastic deformation. Measuring the thickness reduction of the Nb layers provides additional insights into ductile fracture, as demonstrated for Cu-Nb multilayers in Ref. [54] and for dislocation-interface interactions in multilayered metals in Ref. [53].

The individual layers in the upper left section are displaced massively from those in the lower right, indicating severe deformation. A detailed investigation of the region marked in Fig. 8d reveals that this displacement results in complete shear failure of the Nb layers, while the TiN layers fractured in a brittle manner (Fig. 8e). The high-resolution TEM study (Fig. 8f) of the bilayer interface between Nb and TiN confirms that no delamination or debonding occurred, supporting calculations that indicate a high cohesive strength for TiN/Nb multilayers (Fig. 1c). An inverse FFT of this region (not shown) suggests significant dislocation activity in both Nb and TiN layers.

To contextualize the mechanical performance of TiN/Nb multilayer coatings, we compare them with other ceramic/metal multilayer systems such as TiN/Cu, $Al_2O_3$/Nb, and TiN/Ta [15–17,19–21]. TiN/Cu multilayers, while beneficial for applications requiring high electrical and thermal conductivity, often exhibit compromised mechanical strength due to weaker interfacial bonding between the soft Cu layers and the hard TiN layers. This mismatch can lead to reduced load-bearing capacity and increased susceptibility to deformation under mechanical stress. In contrast, $Al_2O_3$/Nb multilayer coatings leverage the high hardness of $Al_2O_3$ and the toughness of Nb; however, the significant disparity in mechanical properties between these layers can result in interfacial delamination and brittle fracture under stress if not properly engineered. Studies have shown that increasing the $Al_2O_3$ content in such composites can lead to increased brittleness and porosity, adversely affecting tensile strength and ductility. TiN/Ta multilayers have been explored for their potential to combine the hardness of TiN with the ductility of Ta, but challenges remain in achieving optimal interfacial bonding and mechanical performance. TiN/Nb multilayer coatings offer a balanced combination of hardness and ductility. The high hardness and wear resistance of TiN are complemented by the ductility and toughness of Nb, allowing for effective plastic deformation accommodation and improved fracture resistance. The coherent or semi-coherent interfaces achievable in TiN/Nb systems contribute to enhanced load transfer and mechanical stability, making them particularly suitable for applications requiring a combination of hardness and ductility.

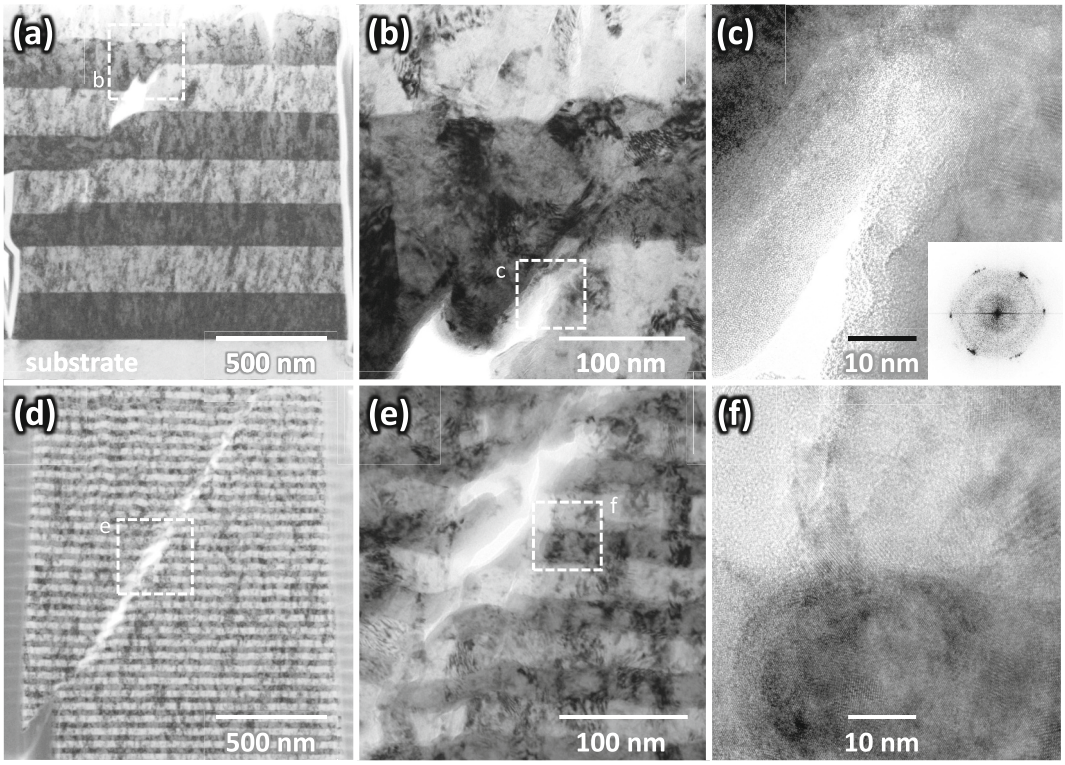


**Fig. 8.** TEM bright-field analysis of the tested 1250-nm-diameter pillar from the TiN/Nb multilayer with $\Gamma = 1$ and bilayer period $\Lambda = 420$ nm **(a–c)** and $\Lambda = 55$ nm **(d–f)**. Detailed views of the regions marked in **(a)** and **(d)** are shown in **(b)** and **(e)**, respectively, while high-resolution TEM (HR-TEM) images of the corresponding marked areas are presented in **(c)** and **(f)**. The inset in **(e)** displays the fast Fourier transform (FFT) of this region. The darker layers represent Nb.

## 4. Summary and conclusions

In this study, 30 multilayered systems consisting of group IV transition metal nitrides (XN) or carbides (XC) and group V–VI high-temperature metals (M) were systematically investigated using DFT calculations to identify material combinations with both structural compatibility and mechanical functionality. The multilayers were designed to combine face-centered cubic ceramics (TiN, ZrN, HfN or TiC, ZrC, HfC) with body-centered cubic metals (V, Nb, Ta, Mo, and W), aiming to achieve (semi-)coherent interfaces that support mechanical integrity and thermal stability under extreme conditions. The selection criteria—negative formation energies, high interface strengths, and significant elastic modulus contrast—enabled the identification of TiN/Nb and TiN/V as the most promising candidates. Owing to its superior oxidation resistance, TiN/Nb was selected for detailed experimental investigations.

The experimental work focused on the synthesis of TiN/Nb multilayers by non-reactive magnetron sputtering, with nitrogen introduced only from the ceramic TiN target during TiN deposition to avoid nitride formation in Nb. Three multilayer series with TiN:Nb layer-thickness ratios ($\Gamma = \ell_{TiN}:\ell_{Nb} = 1$, 3, 6) and bilayer periods ($\Lambda = 51 \pm 4$ nm, 96 $\pm$ 17 nm, and 420 $\pm$ 11 nm) were prepared. X-ray diffraction and selected area electron diffraction analyses confirmed well-separated TiN and Nb layers without indications of fcc-NbN formation, validating the effectiveness of the deposition strategy in maintaining distinct ceramic and metallic phases.

Micropillar compression tests on FIB-fabricated pillars revealed a strong dependence of deformation behavior on both the layer-thickness ratio ($\Gamma$) and bilayer period ($\Lambda$). Multilayers with $\Gamma = 1$ and 3 exhibited pronounced ductility, particularly in pillars with smaller diameters, whereas those with $\Gamma = 6$ showed significantly reduced plasticity. Decreasing $\Lambda$ further suppressed ductile behavior, with multilayers containing thinnest Nb layers exhibiting a transition toward brittle-like failure modes.

A detailed evaluation of the mechanical response confirmed that the confined layer slip (CLS) model captures the dominant deformation mechanisms. The linear relationship between yield strength and inverse layer thickness reflects the layer-constrained dislocation motion, with variations in slope attributed to changes in the active slip systems of Nb. In multilayers with $\Gamma = 6$ and Nb layers as thin as 7 nm, deformation behavior increasingly resembled that of monolithic TiN, as the contribution from the Nb layers diminished.

Overall, the TiN/Nb multilayers with well-chosen layer-thickness ratios and bilayer periods provide critical insight into the interplay between microstructure, interface coherency, and mechanical performance. Multilayers with a balanced ceramic-to-metal ratio combine high strength with enhanced ductility, supporting their use as tough, energy-absorbing coatings for applications in extreme environments. Precise control over individual layer thicknesses proves pivotal in optimizing performance, with potential application areas including turbine rotor blades and wear-resistant surfaces exposed to solid particle erosion.

## CRediT authorship contribution statement

**S. Kagerer:** Writing – original draft, Methodology, Investigation, Formal analysis, Conceptualization. **N. Koutná:** Visualization, Investigation, Formal analysis, Data curation. **L. Zauner:** Data curation. **T. Wojcik:** Methodology, Data curation. **G. Habler:** Data curation. **H. Riedl:** Writing – review & editing, Supervision, Funding acquisition. **P. H. Mayrhofer:** Writing – review & editing, Supervision, Resources, Project administration, Funding acquisition, Formal analysis, Conceptualization. **R. Hahn:** Writing – review & editing, Supervision, Methodology, Formal analysis, Data curation, Conceptualization.

## Declaration of competing interest

The authors declare that they have no known competing financial interests or personal relationships that could have appeared to influence the work reported in this paper.

## Acknowledgments

The authors acknowledge the Austrian research promotion agency (FFG), for the financial support of this study within the "HELOW" project (number: FO999915031), under the e!MISSION funding program, and financial support from the TU Wien Bibliothek through its Open Access funding program. We thank the X-ray Center (XRC) of TU Wien for beam time and the electron microscopy center USTEM TU Wien for access to SEM and TEM facilities. We also appreciate the Faculty of Earth Sciences, Geography, and Astronomy at the University of Vienna for providing access to the FIB-SEM facility. Additionally, we are grateful for the computational resources provided by the Vienna Scientific Cluster (VSC). LZ, HR, and RH gratefully acknowledge funding from the Austrian Federal Ministry Economy, Energy and Toursism, the National Foundation for Research, Technology and Development, and the Christian Doppler Research Association within the framework of the Christian Doppler Laboratory Surface Engineering of High-Performance Components.

## Data availability

Data will be made available on request.

## References

[1] B. Fotovvati, N. Namdari, A. Dehghanghadikolaei, On coating techniques for surface protection: a review, J. Manuf. Mater. Process. 3 (2019) 3010028, https://doi.org/10.3390/jmmp3010028.
[2] A.K. Krella, Degradation of protective PVD coatings, Elsevier Ltd., 2016, 10.1016/B978-0-08-100116-5.00016-8.
[3] P.H. Mayrhofer, C. Mitterer, L. Hultman, H. Clemens, Microstructural design of hard coatings, Prog. Mater Sci. 51 (2006) 1032–1114, https://doi.org/10.1016/j.pmatsci.2006.02.002.
[4] A. Azizpour, R. Hahn, F.F. Klimashin, T. Wojcik, E. Poursaeidi, P.H. Mayrhofer, Deformation and cracking mechanism in CrN/TiN multilayer coatings, Coatings (2019) 9–17, https://doi.org/10.3390/coatings9060363.
[5] R. Hahn, M. Bartosik, R. Soler, C. Kirchlechner, G. Dehm, P.H. Mayrhofer, Superlattice effect for enhanced fracture toughness of hard coatings, Scr. Mater. 124 (2016) 67–70, https://doi.org/10.1016/j.scriptamat.2016.06.030.
[6] N. Koutná, R. Hahn, J. Zálešák, M. Friák, M. Bartosik, J. Keckes, M. Šob, P. H. Mayrhofer, D. Holec, Point-defect engineering of MoN/TaN superlattice films: a first-principles and experimental study, Mater. Des. 108211 (2019), https://doi.org/10.1016/j.matdes.2019.108211.
[7] U. Helmersson, S. Todorova, S.A. Barnett, J.-E. Sundgren, L.C. Markert, J. E. Greene, Growth of single-crystal TiN/VN strained-layer superlattices with extremely high mechanical hardness, J. Appl. Phys. 62 (1987) 481–484, https://doi.org/10.1063/1.339770.
[8] M. Shinn, S.A. Barnett, Effect of superlattice layer elastic moduli on hardness, Appl. Phys. Lett. 64 (1994) 61–63, https://doi.org/10.1063/1.110922.
[9] J.M. Castanho, M.T. Vieira, Effect of ductile layers in mechanical behaviour of TiAlN thin coatings, J. Mater. Process. Technol. 143–144 (2003) 352–357, https://doi.org/10.1016/S0924-0136(03)00454-0.
[10] E. Bemporad, M. Sebastiani, C. Pecchio, S. De Rossi, High thickness Ti/TiN multilayer thin coatings for wear resistant applications, Surf. Coat. Technol. 201 (2006) 2155–2165, https://doi.org/10.1016/j.surfcoat.2006.03.042.
[11] P. Wiecinski, J. Smolik, H. Garbacz, K.J. Kurzydlowski, Microstructure and mechanical properties of nanostructure multilayer CrN/Cr coatings on titanium alloy, Thin Solid Films 519 (2011) 4069–4073, https://doi.org/10.1016/j.tsf.2011.01.183.
[12] J.M. Wheeler, C. Harvey, N. Li, A. Misra, N.A. Mara, X. Maeder, J. Michler, S. Pathak, High temperature nanoindentation of Cu–TiN nanolaminates, Mat. Sci. Eng. A 804 (2021) 140522, https://doi.org/10.1016/j.msea.2020.140522.
[13] N. Li, H. Wang, A. Misra, In situ nanoindentation study of plastic co-deformation in Al-TiN nanocomposites, Sci. Rep. 4 (2014) 6633, https://doi.org/10.1038/srep06633.
[14] Z. Yuan, Y. Han, S. Zang, J. Chen, G. He, Y. Chai, Z. Yang, Q. Fu, Analysis of the mechanical properties of TiN/Ti multilayer coatings using indentation under a broad load range, Ceram. Int. 47 (8) (2021) 10796–10808, https://doi.org/10.1016/j.ceramint.2020.12.196.
[15] L.W. Yang, C. Mayer, N. Li, J.K. Baldwin, N.A. Mara, N. Chawla, J.M. Molina-Aldareguia, J. Llorca, Mechanical properties of metal-ceramic nanolaminates:

effect of constraint and temperature, Acta Mater. 142 (2018) 37–48, https://doi.org/10.1016/j.actamat.2017.09.042.
[16] I.J. Beyerlein, Z. Li, N.A. Mara, Mechanical properties of metal nanolaminates, Annu. Rev. Mater. Res. 52 (2022) 281–304, https://doi.org/10.1146/annurev-matsci-081320-031236.
[17] R. Raghavan, J.M. Wheeler, D. Esqué-de los Ojos, K. Thomas, E. Almandoz, G. G. Fuentes, J. Michler, Mechanical behavior of Cu/TiN multilayers at ambient and elevated temperatures: stress-assisted diffusion of Cu, Mat. Sci. Eng. A 620 (2015) 375–382, https://doi.org/10.1016/j.msea.2014.10.023.
[18] P.H. Mayrhofer, H. Clemens, F.D. Fischer, Materials science-based guidelines to devel-op robust hard thin film materials, Prog. Mater Sci. 146 (2024) 101323, https://doi.org/10.1016/j.pmatsci.2024.101323.
[19] L. Sheng, Y. Xiao, C. Jiao, B. Du, Y. Li, Z. Wu, L. Shao, Influence of layer number on microstructure, mechanical properties and wear behavior of the TiN/Ti multilayer coatings fabricated by high-power magnetron sputtering deposition, J. Manuf. Proc. 70 (2021) 529–542, https://doi.org/10.1016/j.jmapro.2021.09.002.
[20] A. Dück, N. Gamer, W. Gesatzke, M. Griepentrog, W. Österle, M. Sahre, I. Urban, Ti/TiN multilayer coatings: deposition technique, characterization and mechanical properties, Surf. Coat. Technol. 142–144 (2001) 579–584, https://doi.org/10.1016/S0257-8972(01)01171-9.
[21] H. Shang, J. Li, T. Shao, Mechanical properties and thermal stability of TiN/Ta multilayer film deposited by ion beam assisted deposition, Adv. Mat. Sci. Eng. 2014 (2014) 1–8, https://doi.org/10.1155/2014/639461.
[22] R. Hahn, A. Tymoszuk, T. Wojcik, A. Kirnbauer, T. Kozák, J. Čapek, M. Sauer, A. Foelske, O. Hunold, P. Polcik, P.H. Mayrhofer, H. Riedl, Phase formation and mechanical properties of reactively and non-reactively sputtered Ti-B-N hard coatings, Surf. Coat. Technol. 420 (2021) 127327, https://doi.org/10.1016/j.surfcoat.2021.127327.
[23] N. Koutná, A. Brenner, D. Holec, P.H. Mayrhofer, High-throughput first-principles search for ceramic superlattices with improved ductility and fracture resistance, Acta Mater. 206 (2021) 116615, https://doi.org/10.1016/j.actamat.2020.116615.
[24] H. Wang, H. Zeng, Q. Li, J. Shen, Superlattice supertoughness of TiN/MN (M = V, Nb, Ta, Mo, and W): First-principles study, Thin Solid Films 607 (2016) 59–66, https://doi.org/10.1016/j.tsf.2016.03.061.
[25] F. Wang, D. Holec, M. Odén, F. Mücklich, I.A. Abrikosov, F. Tasnádi, Systematic ab initio investigation of the elastic modulus in quaternary transition metal nitride alloys and their coherent multilayers, Acta Mater. 127 (2017) 124–132, https://doi.org/10.1016/j.actamat.2017.01.017.
[26] M.D. Uchic, D.M. Dimiduk, J.N. Florando, W.D. Nix, Sample dimensions influence strength and crystal plasticity, Science 305 (2004) 986–989, https://doi.org/10.1126/science.1098993.
[27] M.D. Uchic, D.M. Dimiduk, R. Wheeler, P.A. Shade, H.L. Fraser, Application of micro-sample testing to study fundamental aspects of plastic flow, Scr. Mater. 54 (2006) 759–764, https://doi.org/10.1016/j.scriptamat.2005.11.016.
[28] D. Kiener, C. Motz, G. Dehm, Micro-compression testing: a critical discussion of experimental constraints, Mater. Sci. Eng. A 505 (2009) 79–87, https://doi.org/10.1016/j.msea.2009.01.005.
[29] G. Dehm, B.N. Jaya, R. Raghavan, C. Kirchlechner, Overview on micro- and nanomechanical testing: new insights in interface plasticity and fracture at small length scales, Acta Mater. 142 (2018) 248–282, https://doi.org/10.1016/j.actamat.2017.06.019.
[30] J.R. Greer, W.D. Nix, Size dependence of mechanical properties of gold at the sub-micron scale, Appl. Phys. A Mater. Sci. Process. 80 (2005) 1625–1629, https://doi.org/10.1007/s00339-005-3204-6.
[31] G. Kresse, J. Furthmüller, Efficient iterative schemes for ab initio total-energy calculations using a plane-wave basis set, J. Phys. Chem. A 124 (2020) 4053–4061, https://doi.org/10.1021/acs.jpca.0c01375.
[32] G. Kresse, D. Joubert, From ultrasoft pseudopotentials to the projector augmented-wave method, Phys. Rev. B 59 (1999) 1758–1775, https://doi.org/10.1103/PhysRevB.59.1758.
[33] W. Kohn, L. Sham, Self-consistent equations including exchange and correlation effects, Phys. Rev. 385 (1965) A1133, https://doi.org/10.1103/PhysRev.140.A1133.
[34] J.P. Perdew, K. Burke, M. Ernzerhof, Generalized gradient approximation made simple, Phys. Rev. Lett. 77 (1996) 3865–3868, https://doi.org/10.1103/PhysRevLett.77.3865.
[35] H.J. Monkhorst, J.D. Pack, Special points for brilloiun- zone integrations, Phys. Rev. B 13 (1976) 5188, https://doi.org/10.1103/PhysRevB.13.5188.
[36] F. Mouhat, F.X. Coudert, Necessary and sufficient elastic stability conditions in various crystal systems, Phys. Rev. B 90 (2014) 224104, https://doi.org/10.1103/PhysRevB.90.224104.
[37] Y. Le Page, P. Saxe, Symmetry-general least-squares extraction of elastic data for strained materials from ab initio calculations of stress, Phys. Rev. B 65 (2002) 104104, https://doi.org/10.1103/physrevb.65.104104.
[38] R. Yu, J. Zhu, H.Q. Ye, Calculations of single-crystal elastic constants made simple, Comput. Phys. Commun. 181 (2010) 671–675, https://doi.org/10.1016/j.cpc.2009.11.017.
[39] P. Lazar, J. Redinger, R. Podloucky, Density functional theory applied to VN/TiN multilayers, Phys. Rev. B 76 (2007) 174112, https://doi.org/10.1103/PhysRevB.76.174112.
[40] P. Řehák, M. Černý, D. Holec, Interface-induced electronic structure toughening of nitride superlattices, Surf. Coat. Technol. 325 (2017) 410–416, https://doi.org/10.1016/j.surfcoat.2017.06.065.
[41] R. Hill, The elastic behaviour of a crystalline aggregate, Proc. Phys. Soc. A 65 (1952) 349–354, https://doi.org/10.1088/0370-1298/65/5/307.
[42] L. Zauner, R. Hahn, E. Aschauer, T. Wojcik, A. Davydok, O. Hunold, P. Polcik, H. Riedl, Assessing the fracture and fatigue resistance of nanostructured thin films, Acta Mat. 239 (2022) 118260, https://doi.org/10.1016/j.actamat.2022.118260.
[43] A. Wagner, D. Holec, P.H. Mayrhofer, M. Bartosik, Enhanced fracture toughness in ceramic superlattice thin films: on the role of coherency stresses and misfit dislocations, Mater. Des. 202 (2021) 109517, https://doi.org/10.1016/j.matdes.2021.109517.
[44] J. Buchinger, N. Koutná, Z. Chen, Z. Zhang, P.H. Mayrhofer, D. Holec, M. Bartosik, Toughness enhancement in TiN/WN superlattice thin films, Acta Mat. 172 (2019) 18–29, https://doi.org/10.1016/j.actamat.2019.04.028.
[45] Z. Zhang, A. Ghasemi, N. Koutná, Z. Xu, T. Grünstäudl, K. Song, D. Holec, Y. He, P. H. Mayrhofer, M. Bartosik, Correlating point defects with mechanical properties in nanocrystalline TiN thin films, Mater. Des. 207 (2021) 109844, https://doi.org/10.1016/j.matdes.2021.109844.
[46] K. Zhang, K. Balasubramanian, B.D. Ozsdolay, C.P. Mulligan, S.V. Khare, W. T. Zheng, D. Gall, Growth and mechanical properties of epitaxial NbN(001) films on MgO(001), Surf. Coat. Technol. 288 (2016) 105–114, https://doi.org/10.1016/j.surfcoat.2016.01.009.
[47] J.R. Greer, W.D. Nix, Nanoscale gold pillars strengthened through dislocation starvation, Phys. Rev. B 73 (24) (2006) 245410, https://doi.org/10.1103/PhysRevB.73.245410.
[48] D. Tabor, A simple theory of static and dynamic hardness, Proc. R. Soc. Lond. A Math. Phys. Sci. 192 (1948) 247–274, https://doi.org/10.1098/rspa.1948.0008.
[49] I. El Azhari, J. Garcia, M. Zamanzade, F. Soldera, C. Pauly, L. Llanes, F. Mücklich, Investigations on micro-mechanical properties of polycrystalline Ti(C, N) and Zr(C, N) coatings, Acta Mat. 149 (2018) 364–376, https://doi.org/10.1016/j.actamat.2018.02.053.
[50] H. Umezawa, M. Yamanaka, N. Nishida, Statistical Evaluation of Mechanical Properties of RRR300 Niobium Sheets, JACoW IPAC2024 (2024) THPS64 3897–3900, doi:10.18429/JACoW-IPAC2024-THPS64.
[51] W.A. Spitzig, C.L. Trybus, F.C. Laabs, Structure properties of heavily cold-drawn niobium, Mat. Sci. Eng. A 145 (1991) 179–187, 0921-5093/91/$3.50.
[52] W.D. Nix, Mechanical properties of thin films, Metall. Trans. A 20 (11) (1989) 2217–2245, https://doi.org/10.1007/BF02666659.
[53] D. Bhattacharyya, N.A. Mara, P. Dickerson, R.G. Hoagland, A. Misra, Compressive flow behavior of Al-TiN multilayers at nanometer scale layer thickness, Acta Mat. 59 (2011) 3804–3816, https://doi.org/10.1016/j.actamat.2011.02.036.
[54] A. Misra, J.P. Hirth, R.G. Hoagland, Length-scale-dependent deformation mechanisms in incoherent metallic multilayered composites, Acta Mat. 53 (2005) 4817–4824, https://doi.org/10.1016/j.actamat.2005.06.025.
[55] W.D. Nix, Yielding and strain hardening of thin metal films on substrates, Scr. Mater. 39 (1998) 545–554, https://doi.org/10.1016/S1359-6462(98)00195-X.
[56] G.I. Taylor, The mechanism of plastic deformation of crystals. Part I. Theoretical considerations, Proc. R. Soc. London. Series A, Math. Phys. Sci. 145(855) (1934) 362–387, doi:10.1098/rspa.1934.0188.
[57] A.K. Singh, H.-P. Liermann, Strength and elasticity of niobium under high pressure, J. App. Phys. 109 (2011) 113539, https://doi.org/10.1063/1.3594748.